NANO LETTERS
Cite This: Nano Lett. XXXX, XXX, XXX−XXX
Letter
pubs.acs.org/NanoLett

Metasurface Mirrors for External Control of Mie Resonances

Jorik van de Groep and Mark L. Brongersma*

Geballe Laboratory for Advanced Materials, Stanford University, 476 Lomita Mall, Stanford, California 94305, United States

Supporting Information

ABSTRACT: The ability to control and structurally tune the optical resonances of semiconductor nanostructures has far-reaching implications for a wide range of optical applications, including photodetectors, (bio)sensors, and photovoltaics. Such control is commonly obtained by tailoring the nanostructure's geometry, material, or dielectric environment. Here, we combine insights from the field of coherent optics and metasurface mirrors to effectively turn Mie resonances on and off with high spatial control and in a polarization-dependent fashion. We illustrate this in an integrated device by manipulating the photocurrent spectra of a single-nanowire photodetector placed on a metasurface mirror. This approach can be generalized to control spectral, angle-dependent, absorption, and scattering properties of semiconductor nanostructures with an engineered metasurface and without a need to alter their geometric or materials properties.

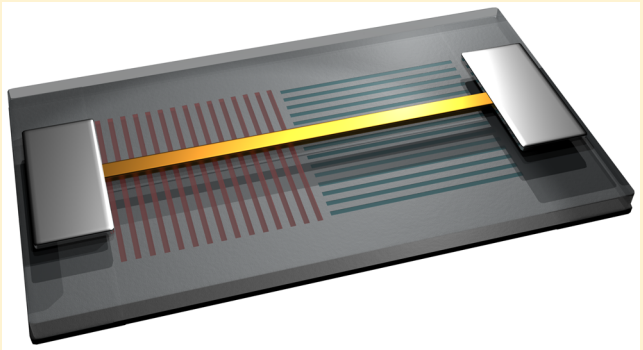

KEYWORDS: *Mie resonance, metasurface mirror, semiconductor nanowire, nanoscale photodetector, plasmon*

Nanostructures with a high refractive index can support strong optical resonances in the visible spectral range.[1,2] These dielectric (Mie) resonances[3] give rise to large optical cross sections that are now applied in a wide range of applications; including directional scattering,[4−8] spectrally selective absorptive layers,[9,10] optical coatings for photovoltaic cells,[11−15] wavefront shaping,[16−18] and nonlinear optics.[19−23] The use and manipulation of such optical resonances is therefore at the heart of the field of nanophotonics. For dielectric resonators this tuning is typically done by varying the nanostructure size,[24,25] shape,[26] and dielectric constant of the environment[24,25] or resonator material.[27] The field of coherent optics[28] has brought a new angle to control and enhance light-matter interaction. For example, by strategically placing ultrathin films in electric field maxima or minima of optical standing wave patterns light absorption can be enhanced or suppressed, respectively.[29−32] As high-refractive index nanostructures are also small compared to the wavelength a similar principle can be applied to control the excitation of a desired optical mode.[33] Here, we show that metamaterial mirrors[34−36] enable the use of this concept in an integrated device by offering a full 2π reflection phase control. By controlling the nanopatterning, the local reflection phase can be tuned to turn on and off resonances with high spatial control and in a polarization-dependent fashion. The resulting control over the resonant light absorption is demonstrated in established photocurrent measurement techniques on individual semiconductor nanowires (NWs).[37−44] This general approach can be used to control spectral, angle-dependent, absorption, and scattering functionality of a metasurface and greatly enhance their applicability.

Results. *Metamirror for External Control of Resonances.* Figure 1 illustrates how polarization-dependent metasurface back reflectors can manipulate the resonant excitation amplitude of a Si NW by placing it in the vicinity. The Si NW (red) is illuminated by a plane wave polarized along the axis of the NW (defined as TM), and supports a strong optical resonance for $\lambda \sim 575$ nm. It is positioned 600 nm above a metasurface mirror composed of a grooved silver mirror oriented parallel (Figure 1a) or perpendicular (Figure 1b) to the NW axis (see Supporting Figure S1 for a summary of the geometry). For the parallel orientation, the incident light reflects off the metasurface mirror analogous to a flat mirror and picks up a $\sim\pi$ reflection phase. The resulting standing wave profile couples to the resonant mode in the NW (Figure 1c), giving rise to a high field intensity inside the wire and thereby strong resonant absorption (Figure 1f). In contrast, for the perpendicular groove orientation the incident light couples to metal−insulator−metal (MIM) gap plasmon modes[45] in the grooves (Figure 1d,e). The phase pick-up upon reflection increases substantially, as can intuitively be understood from the propagation phase of the MIM plasmon as it propagates to the bottom of the groove and back after reflecting from the bottom. Hence, by carefully engineering the path length (groove depth) and MIM mode index (groove width) the metamirror phase pick-up can be tuned completely at will and across a full 2π.[35] We use this to offset the standing wave profile (compare Figure 1c−e) and minimize the excitation of the

Received: March 21, 2018
Revised: May 10, 2018
Published: May 22, 2018

DOI: 10.1021/acs.nanolett.8b01148
Nano Lett. XXXX, XXX, XXX−XXX

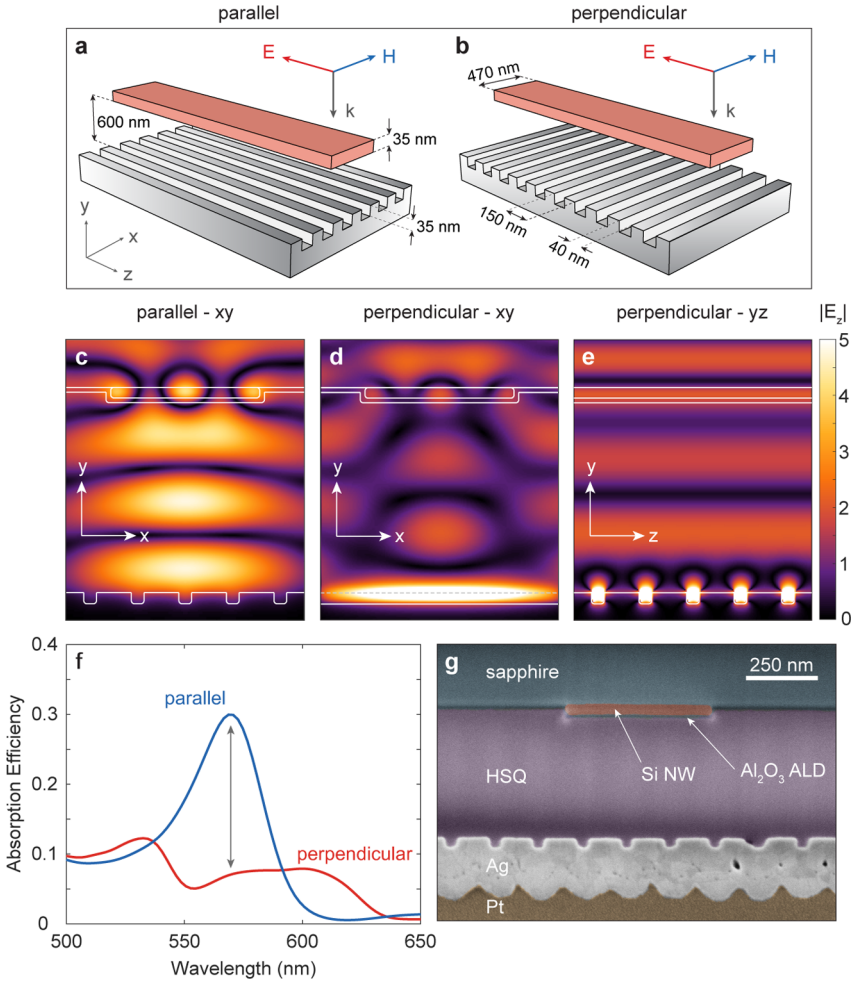

Figure 1. Controlling dielectric resonances through metasurface back reflectors. (a,b) Schematic of optically resonant Si NW excited by a plane wave polarized along wire axis (*z*-axis). The NW is positioned above metamirror with grooves oriented either parallel (a) and perpendicular (b) to wire axis. (c) Simulated $|E_z|$ field distribution (λ = 575 nm) for grooves parallel to NW axis (*xy*-plane in a) showing enhanced resonant excitation of the NW through coupling to the standing wave profile above metamirror. (d,e) $|E_z|$ field distribution for grooves perpendicular to the NW axis (*xy*-plane (d) and *yz*-plane (e) in b). The standing wave profile is offset as result of light coupling to gap plasmons in grooves of the metamirror, suppressing the resonant excitation of the NW. Note: color scale in panels d and e is saturated to match c. (f) Simulated absorption efficiency spectra for Si NWs above metamirror with grooves oriented parallel (blue) and perpendicular (red) to NW axis. (g) False color SEM image of FIB cross section of as-fabricated device with different layers labeled. The Pt is deposited to improve the cross-section quality.

resonant mode in the NW, thereby suppressing the resonant absorption (Figure 1f). Comparing the absorption efficiencies (defined as the ratio of the absorption cross section and geometrical cross section) at resonance demonstrates how the metamirror orientation changes the absorption efficiency by a factor 4.3 by controlling the resonant excitation amplitude. To demonstrate this experimentally, we fabricate contacted Si NWs combined with the complex three-dimensional (3D) metasurface/spacer nanostructure and use the photocurrent generated in the semiconductor NW as a local (near-field) probe of the absorption efficiency. Figure 1g shows a focused-ion beam (FIB) cross section of an as-fabricated device with the Si NW judiciously positioned above a nanopatterned metasurface back reflector and embedded in hydrogen silsesquioxane (HSQ), a lossless dielectric with an index $n \sim 1.40$.

Single Nanowire Optical Characterization. Before we analyze the performance of the completed device, we first study the resonant optical properties of a bare Si NW on a sapphire substrate in air. Figure 2a,c shows the simulated backscattering (a) and absorption (c) efficiency of an infinitely long 490 nm wide Si NW (35 nm high). The backscattering efficiency is defined as the ratio of the backscattering cross section and the geometrical cross section. The dielectric (Mie) resonance of the NW is slightly blue-shifted in air with respect to the same NW embedded in HSQ in our finished devices. For easy comparison, we use a slightly wider (490 nm instead of 470 nm) NW in these experiments to maintain the resonance at $\lambda \sim 575$ nm. A clear resonant peak in absorption is observed for TM polarization (Figure 2c), whereas a nonresonant background absorption is observed for TE polarization. The modal field profile of this TM_{31} resonance[46] (inset Figure 2a) is characterized by three (one) antinodes in the in-plane (vertical) direction, respectively. This field profile results as incident light scatters from the edges of the NW and couples to a guided mode propagating in the *x*-direction. The reflection from the NW edges then sets up a standing wave inside the wire. The absorption resonance gives rise to a distinctive asymmetrical Fano line shape in the backscattering efficiency (Figure 2a), which is a result of interference between light scattered by the resonant pathway and light directly reflected from the NW

DOI: 10.1021/acs.nanolett.8b01148
Nano Lett. XXXX, XXX, XXX−XXX

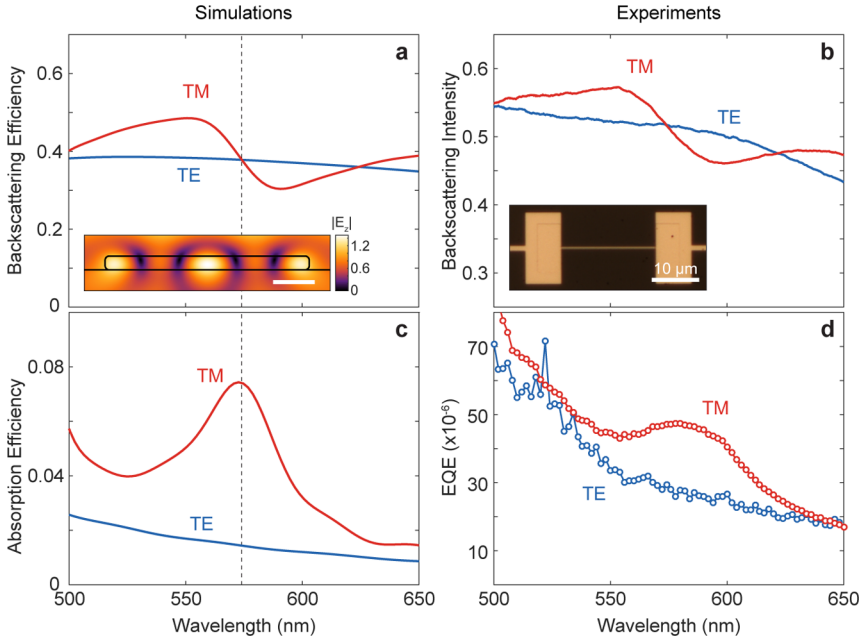

Figure 2. Dielectric resonance of Si NW on sapphire substrate. (a,c) Simulated backscattering efficiency (a) and absorption efficiency (c) of a Si NW with w = 490 nm and h = 35 nm on a sapphire substrate for TM (red) and TE (blue) polarization. Resonantly enhanced absorption is observed for TM polarization (λ = 575 nm), which gives rise to an asymmetric Fano line shape in the backscattering spectrum. The simulated modal field profile at resonance is shown as an inset to panel a (scale bar: 100 nm). (b) Experimentally measured bright-field backscattering intensity for TM (red) and TE (blue) polarization, clearly showing the asymmetrical resonant line-shape. Inset: optical microscopy image of a 20 μm long contacted Si NW. (d) EQE spectra for TM and TE polarized excitation, as obtained from single-NW photocurrent measurements. A clear peak in the EQE is observed for TM polarization as a result of resonant absorption.

surface.[47] The undulation in the scattering spectrum is centered at the absorption resonance, consistent with Fano interference.

To study the bare Si NWs experimentally, we fabricate contacted Si NWs on a sapphire substrate. We etch c-Si on sapphire down to 35 nm thickness and pattern the thin Si film into NWs through electron-beam lithography (EBL) and etching. We then fabricate two 100 nm-thick Al contact pads using a second EBL step, physical vapor deposition, and lift-off process. See Methods and steps 1−5 in Supporting Figure S6 for details. The resulting NWs are 20 μm long and uniform in width, as confirmed with SEM inspection (Figure 3a). Figure 2b shows the measured backscattering intensity, normalized to the reflectance of a silver mirror (see Methods and Supporting Figure S2). We show a microscope image of the contacted NW as an inset. Indeed, a clear asymmetrical Fano line shape is observed around $\lambda \sim$ 575 nm for TM polarization, which is in very good qualitative agreement with the simulated back-scattering spectra (Figure 2a). For TE polarization on the other hand, a flat back scattering spectrum is observed. In order to demonstrate resonant absorption, we use the generated photocurrent as a local probe of the absorption in the NW. Using a home-built setup, we measure the photocurrent from the NW, while controlling the illumination wavelength, intensity, polarization, and spatial position of an optical excitation spot (see Methods and Supporting Figure S3). The off-normal angles of incidence up to 25° as a result of the numerical aperture of the objective (0.42) give rise to a small decrease in amplitude but no spectral shift of the optical resonance (see Supporting Figure S4). The external quantum efficiency (EQE), defined as the ratio of the number of extracted electrons and illumination photons, shows a clear peak for TM-polarized excitation as a result of resonant absorption (Figure 2d), while the EQE for TE polarization only shows intrinsic background absorption. Altogether, these results demonstrate that the single NW supports a clear dielectric resonance and the EQE is a good measure of the resonant absorption inside the NW.

Metamirror Fabrication. After characterization of the NW in air, we fabricate a thick oxide spacer layer and Ag metasurface mirror on top of the Si NWs (Figures 1g and 3). See Methods and Supporting Figure S6 steps 6−9 for details. First, we overcoat the contacted Si NWs (Figure 3a) with a thick layer of HSQ. We optimize the thickness of the HSQ to spectrally overlap the Fabry−Pérot and Mie resonance (see Supporting Figure S5). Next, we use the fact that HSQ serves as a negative-tone e-beam resist to pattern it into a pad on top of the NW devices (Figure 3b, purple). This leaves the contact pads free for easy wire bonding to the outside world. In a following step, we use a 35 nm thin layer of HSQ to fabricate the high-resolution metasurface pattern (40 nm lines of HSQ, 150 nm period) on top of the HSQ spacer by EBL. Finally, the (meta)mirror is completed by overcoating the HSQ patterns locally with 225 nm of Ag. The completed samples are composed of 7 NW devices covered by the 3D metasurface mirrors (Figure 3b).

The metamirror is composed of two orthogonal 10 μm × 10 μm domains, which are easily observable from the top (back) side of the mirror both by SEM imaging (Figure 3c) and optical microscopy (Figure 3d,e). To understand why, we show a high-resolution FIB cross section of the metamirror as an inset to Figure 3c. The square cross-sectional shape of the grooves is clearly seen and the Ag overcoating is highly conformal. Typical grooves dimensions obtained from FIB cross sections are w = 40 nm, and h = 35 nm. The shape of the grooves propagates through the deposited Ag layer and results into an undulating top surface (Figure 3c, inset). This gives rise to plasmonic

DOI: 10.1021/acs.nanolett.8b01148
Nano Lett. XXXX, XXX, XXX−XXX

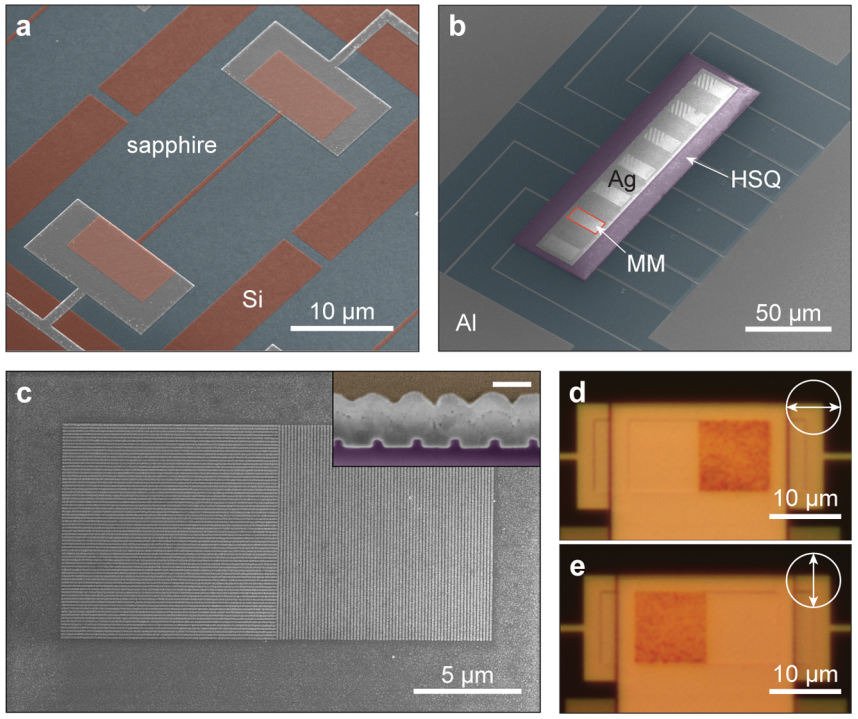

Figure 3. Fabrication of single contacted Si NWs and metasurface back reflectors. (a) False color SEM image of a fabricated single Si NW (red) on sapphire (blue), contacted by Al contacts (gray/white). (b) False-color SEM of a completed device with seven NW devices covered by an HSQ pad (purple) and silver (metasurface) mirror. The red box outlines the metasurface domains shown in c. (c) SEM image of top surface of the metamirror. The two metasurface domains with perpendicular lines are clearly visible as a result of the conformal deposition of the Ag. Inset: false-color SEM image of FIB cross section of the metamirror (scale bar is 150 nm), showing the high-resolution metasurface at the interface with the HSQ (purple) and conformal roughness at interface with Pt (yellow) that was deposited for improved cross-section quality. (d,e) Optical microscope image of the top Ag surface with the incident polarization parallel (d) and perpendicular (e) to NW axis (indicated by arrows in top right corner). Contrast due to plasmonic absorption is clearly observable demonstrating the polarization-dependent performance of the metasurface pattern.

absorption in the grooves.[45] Even though we did not intentionally optimize the groove pattern on the backside of the film, polarization-controlled optical microscope image clearly show the polarization-dependent properties we expect from our metamirror: domains with grooves oriented perpendicular to the incident polarization show a brownish color as a result of plasmonic absorption, whereas the parallel oriented domains show the same color as the surrounding flat mirror. Finally, a FIB cross section of the completed device shows the true 3D geometry of the device (Figure 1g) and verifies the 580 nm thickness of the HSQ spacer as well as the 15 nm thick conformal protective ALD layer around the Si NW. The thickness of the spacer layer was further confirmed by reflection measurements of the Fabry-Pérot resonance of the continuous Si located directly next to the wire (see Figure 3a) and comparison with transfer-matrix calculations (Supporting Figure S7).

Photocurrent Measurements of Completed Devices. Local photocurrent measurements of the completed devices demonstrate the external control over the resonance amplitude by the metamirror geometry. We illuminate the completed devices through the sapphire substrate. To compensate for the nonzero birefringence of the sapphire, we rotate a second corrective substrate by 90° and mount it on the bottom (see Methods and Supporting Figure S6, step 9 for details). Then, we confirm/calibrate the polarization of the incident light after propagation through the two substrates using the polarization-dependent reflectance of the metasurface domains (see Supporting Figure S8). Figure 4a shows the EQE spectra (TM-polarization) for the NW measured at the centers of the two different metamirror domains. An optical microscope image of the completed device (unpolarized light) is shown as an inset with the location of the measured spectra indicated. Indeed, a clear resonant peak in the photocurrent is observed at $\lambda \sim 575$ nm for the parallel orientation of the grooves (blue). The higher quality factor of the absorption resonance compared to the NW in air (Figure 2d) is a clear demonstration that the resonantly enhanced absorption results from the presence of the metamirror. Note that the spectra (Figure 2d and Figure 4a) cannot be compared on an absolute scale due to strong variations in the carrier collection efficiency. For the perpendicular orientation (red) on the other hand, the peak in the EQE is strongly suppressed into a weak shoulder on the sloped background absorption. A comparison of the EQE spectra (Figure 4a) demonstrates how the presence of an engineered metamirror in the dielectric environment of a resonant Si NW can effectively suppress/switch off the resonance in a spatially controlled manner.

Concurrently measured spatial maps of the reflection and photocurrent at resonance ($\lambda \sim 575$ nm, TM) show the strongly localized photocurrent hot spot near the left contact (Figure 4b,c). Although the metamirror domains are uniform (b), the charge carrier collection efficiency of the NW photodetector is most efficient at the junction between the left Al contact and the Si wire (c). We attribute this to local band bending of the (undoped, intrinsic) Si and use the fact that the hot spot relocates to the other contact for reversed

DOI: 10.1021/acs.nanolett.8b01148
Nano Lett. XXXX, XXX, XXX−XXX

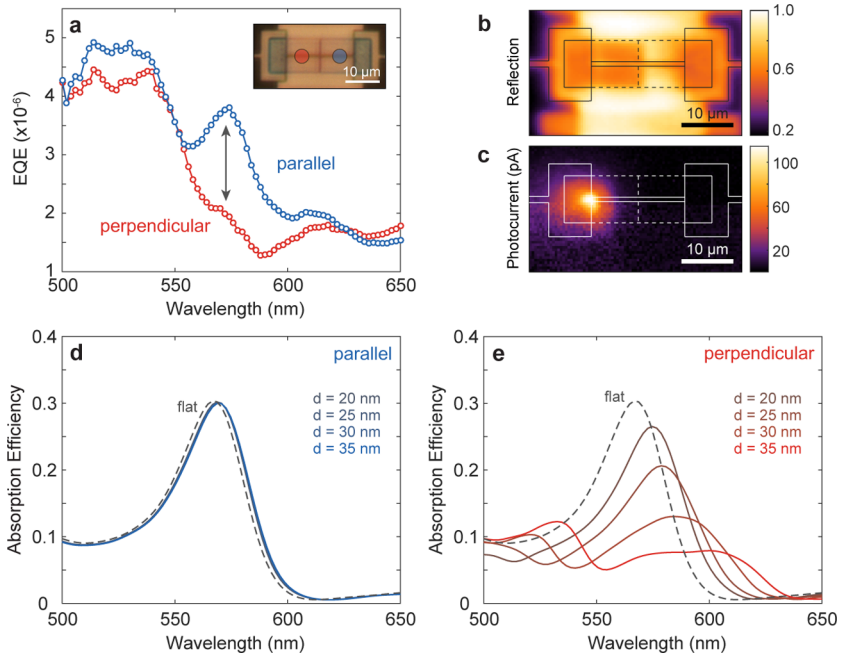

Figure 4. Experimental demonstration of metamirror-controlled resonant absorption. (a) Measured EQE spectra of a Si NW above metamirror illuminated through the sapphire substrate with TM polarization (along NW axis). A peak in photocurrent is observed for grooves parallel to the NW axis (blue) as a result of enhanced resonant absorption, while photocurrent is suppressed for the perpendicular orientation (red), analogous to the simulated absorption efficiency (Figure 1f). Inset: optical microscope image through sapphire substrate, red and blue dots indicate locations where spectra were measured. (b,c) Spatial map of reflection (b) and photocurrent (c) at resonance (λ = 575 nm), measured simultaneously. The polarization-dependent reflectance of the metamirror domains is clearly visible (b). The photocurrent map shows most efficient charge carrier extraction close to one of the contacts (c). (d,e) Simulated absorption efficiency of the Si NW above a metamirror with increasing groove depth (40 nm groove width, 150 nm pitch) oriented parallel (d) and perpendicular (e) to NW axis. Absorption efficiency above a flat mirror is also shown as a reference (gray, dashed). No significant change is observed for the parallel orientation whereas increased phase pickup of the metamirror with increasing groove depth redshifts the Fabry-Pérot resonance away from the NW resonance for the perpendicular orientation.

external bias to collect the spectrum of the other domain with a high signal-to-noise ratio.

To corroborate the polarization-dependent control over the NW resonance excitation efficiency, Figure 4d,e show the simulated absorption efficiency of the Si NW above the metamirror domain for increasing groove depth. For parallel orientation (d, no coupling to MIM modes), the metamirror strongly resembles the performance of a flat mirror. No visible change in the absorption efficiency is observed for increased groove depth. For the perpendicular orientation on the other hand (e), a notable change in the absorption efficiency is observed for an increased groove depth. Deeper grooves result in longer path length for the gap plasmons in the groove, giving rise to an increased reflection phase of the metamirror. Indeed, the Fabry-Pérot peak redshifts away from the NW resonance to $\lambda \sim 620$ nm, causing an offset in the standing wave profile at $\lambda \sim 575$ nm (Figure 1d,e). Minimized coupling to the NW dielectric resonance is observed for 35 nm deep grooves, showing how the metamirror geometry can be used to control the resonant excitation efficiency and spectral properties.

Discussion. Using photocurrent and reflection measurements, we have demonstrated how engineered metasurface mirrors can be used to locally enhance/suppress the resonant excitation of a semiconductor nanowire in a polarization-dependent fashion. The same concept can be used to control the resonance wavelength (see Supporting Figure S9), and angular scattering profile. Spatially controlled metamirrors can be generalized to applications in spectrum splitting for parallel tandem (nanoscale) solar cells, as well as functionalized electrodes for spectrally selective light-emitting diodes. Moreover, recent developments in nanoimprint lithography[48] enable cost-effective large-area applications of nanopattered metasurface mirrors in devices with enhanced functionality.

Methods. *Device Fabrication.* Devices are fabricated in two stages. First, contacted Si NWs are fabricated on a sapphire substrate (Figure S6, steps 1−4). Second, the metamirror is fabricated at a well-defined height above the NW (Figure S6, steps 5−8). In the following, the numbers refer to the steps in Figure S6. All e-beam lithography (EBL) steps are performed using a JEOL JBL 6300 100 kV system and a conductive polymer top coating (e-spacer) to prevent charging effects in the nonconductive substrate.

(1) c-Si (500 nm thick) on sapphire is obtained commercially (MTI-corp). (2) After substrate cleaning, the c-Si is etched to 34 ± 2 nm by reactive-ion etching using a mixture of Cl_2 and HBr, and cleaned again. (3) One hundred nanometers thick Au alignment markers are fabricated through EBL. To do this, a bilayer of (positive-tone) MMA (MMA(8.5)MAA EL6) and PMMA (495PMMA A 4) is spin coated, exposed, and developed in MIBK/IPA 1:1. Next, 5 nm of Ti and 100 nm of Au are deposited through e-beam evaporation, and lift-off is performed in acetone at 45 °C. (4) The Si layer is patterned into NWs by a second step of EBL followed by reactive ion etching. CSAR (SX AR-P 6200/2, 9% in Anisole, positive-tone) is spin coated, exposed, and developed in xylenes. Next, the thin Si layer is anisotropically etched with a mixture of CHF_3 and SF_6, followed by resist stripping using Remover PG at 65 °C and sample cleaning. (5) Al contact pads to the Si NWs are fabricated through a third step of EBL, using the same process as step 3, except that 100

DOI: 10.1021/acs.nanolett.8b01148
Nano Lett. XXXX, XXX, XXX−XXX

nm of Al is deposited through e-beam evaporation instead of Ti/Au. We used current−voltage measurements to confirm that the contacts between the aluminum and silicon are ohmic in the −300 to 300 mV range with R = 53.8 MΩ.

(6) To protect the Al contacts from chemically incompatible developers in the rest of the process, a 15 nm protective layer of Al_2O_3 is deposited conformally over the entire sample using thermal atomic-layer deposition (ALD) at 150 °C. Next, a thick (580 nm) hydrogen silsesquioxane (HSQ, Fox 16) spacer is deposited locally through a fourth EBL step. Five hundred and eighty nanometers of Fox 16 flowable oxide (negative-tone) is deposited through accurate control over the spin speed, followed by exposure and development in TMAH (25% in water). (7) To fabricate oxide-filled grooves in the metasurface mirror, the high-resolution metasurface pattern is fabricated on top of the HSQ spacer using a thin layer of HSQ and a fifth step of EBL. HSQ (XR-1054−004, 4% in MIBK) is further diluted with MIBK to 2%, and spin-coated to form a 35 nm thick layer on top of the thick HSQ layer. Next, 10 μm × 10 μm metasurface domains (40 nm wide lines, 150 nm pitch) are written in the resist, followed by a development process analogous to step 6. (8) Finally, the metasurface mirror is completed by locally overcoating the HSQ pattern with an opaque layer of Ag. This is performed in two steps to prevent lift-off problems. First, a bilayer of MMA (MMA(8.5)MAA EL6) and thick PMMA (950PMMA A 4) is spin coated and patterned through a sixth round of EBL, analogous to step 2. A 125 nm thick of Ag film is then deposited conformally through sputter coating, followed by lift-off in acetone at 45 °C. Second, to make the Ag layer opaque a seventh EBL step (analogous to step 3) is used, followed by e-beam evaporation of 100 nm of Ag.

After fabrication, a 3 nm Al_2O_3 layer is deposited conformally over the entire sample using thermal atomic-layer deposition (ALD) at 90 °C to prevent oxidation of the Ag mirror. (9) The completed devices are illuminated through the sapphire substrate, which has an anisotropy in the refractive index of 0.008.[49] To maintain linear polarization after propagation through the substrate and enable imaging through the substrate, a second substrate from the same batch is stripped from its c-Si (using process in step 2) to obtain a bare sapphire substrate. This corrective substrate is rotated 90° and mounted on the backside of the sample substrate, such that the polarization-dependent phase-delay in the first substrate is compensated in the second. To this end, a thermoplastic (pink in Figure S6) is used to seal the edges, and the gap between the substrates is filled with index-matching oil (n = 1.77). Finally, the samples are mounted and wire-bonded to a sample holder for electro-optical measurements.

Bright-Field Backscattering Measurements. Bright-field backscattering spectra of the NW in air are measured using a Nikon C1 confocal microscope (see Figure S2). Light from a halogen lamp is first polarized using a rotatable polarizer and sent to the sample through a 50× objective (Nikon LU Plan Fluor, *NA* = 0.8, 1 mm working distance). Broadband wide-field illumination is used with the aperture stop closed to obtain minimally focused excitation with angles of incidence close to normal. A confocal scanner with a 30 μm pinhole is used to spatially select the backscattering signal of the NW, which is analyzed using a SpectraPro 2300i spectrometer (150 lines/mm, blazed for λ = 500 nm) and Pixis Si CCD (−70 °C detector temperature). The reported spectra are the average of 15 frames (2 s integration time each). The spectra are normalized to the reflection spectrum of a protected silver mirror (Thorlabs, PF10-03-P01).

Photocurrent Measurements. Photocurrent measurements are performed using a home-built optoelectronic setup (see Figure S3). A supercontinuum laser and acousto-optic tunable filter (both Fianium) are used to tune the wavelength of the monochromatic illumination (∼5 nm bandwidth). A mechanical chopper wheel (400 Hz) is used to modulate the laser light, after which two achromatic lenses and a 30 μm pinhole are used to improve the spot shape. A broadband polarizer and an automated broadband half-wave plate are used to control the input polarization. A 50× long working distance (Mitutoyo M Plan APO NIR, NA = 0.42, 20 mm working distance) focuses the light onto the sample. The spot size (fhwm) at λ = 575 nm is 1.59 ± 0.02 and 2.94 ± 0.11 μm when illuminated from air or through the sapphire substrates respectively, as determined from knife-edge measurements. An imaging system with two 50:50 beam splitters (on flip mounts), a halogen lamp with diffuser, and CCD imaging camera with tube lens are used to image the sample. A glass slide directs a small fraction of the reflected laser light onto a large-area Si photodiode (New Focus, model 2031), connected to a lock-in amplifier (Stanford Research SR810 DSP), to measure the reflection signal. The sample is mounted on a three-axis piezo stage to accurately control the spatial position of the focused laser on the sample. A sourcemeter (Keithley 2612) is connected in series with a tunable current-to-voltage amplifier and the wire-bonded sample and applies a dc bias (typically 250 mV) to extract the generated charge-carriers. The modulated amplifier output voltage is sent to a second lock-in amplifier (Stanford Research SR810 DSP) to measure the photocurrent. The internal collection efficiency is typically maximized close to one of the contacts (Figure 4c). To measure the photocurrent on the other side of the wire, the polarity of the external bias is switched to relocate the maximum collection efficiency to the other contact. To calculate the EQE, the power spectrum at the position of the sample is measured using a calibrated power meter (Thorlabs, PM-100USB).

FDTD Simulations. Finite-difference time-domain simulations are performed using commercial software (Lumerical[50]). For the wire in air (Figure 2), 2D simulations are used with perfectly matched layers (PML) on all sides and a mesh size of 1 nm. A Si NW (490 nm wide, 35 nm high) with rounded corners (10 nm radius) is positioned on a sapphire (modeled as n = 1.77). A total-field scattering field (TFSF) source is used to illuminate with a plane wave (λ = 400−900 nm). A flux box around the wire in the full-field is used to calculate the absorption efficiency, while only the scattered field in the upper hemisphere is used to calculate the backscattering efficiency.

A similar method is used for the completed devices (Figure 1 and Figure 4) except that simulations are performed with a background index of n = 1.77 to simulate light incident through the sapphire superstrate. For the perpendicular groove-orientation 3D simulations with a 2 nm mesh are used with PMLs in the *xy*-plane and periodic boundary conditions in the *z*-plane. A Si NW (470 nm wide, 35 nm high) with rounded corners (10 nm radius) is positioned at the surface of the superstrate and a 15 nm conformal coating of Al_2O_3 is included (see Figure S1). A 600 nm thick layer of HSQ (Fox 16) is used to match the measured interference maximum at λ = 575 nm (see Figure S4 and Figure S6). To simulate the metasurface mirror, a silver substrate with 40 nm wide grooves (35 nm

DOI: 10.1021/acs.nanolett.8b01148
Nano Lett. XXXX, XXX, XXX−XXX

deep) with rounded bottom corners (10 nm radius) is used (period of 150 nm).

Optical constants for Ag are obtained from a combined Drude, Lorentz, and Debye model fitted to the data from Palik,[51] optical constants for Si are also taken from Palik. Optical constants for HSQ (Fox 16 flowable oxide) are obtained from spectroscopic ellipsometry ($n \sim 1.4$).

■ ASSOCIATED CONTENT

Supporting Information

The Supporting Information is available free of charge on the ACS Publications website at DOI: 10.1021/acs.nanolett.8b01148.

Supporting Figures S1−9 describing simulations layout, schematics of experimental setups, fabrication scheme, influence of focusing on resonant excitation, spacer thickness optimization and calibration, polarization calibration, and demonstration of wavelength tuning with metamirror devices (PDF)

■ AUTHOR INFORMATION

Corresponding Author

*E-mail: brongersma@stanford.edu.

ORCID

Jorik van de Groep: 0000-0003-3033-8005

Mark L. Brongersma: 0000-0003-1777-8970

Author Contributions

J.vdG. and M.L.B. conceived the research idea. J.vdG. performed the device fabrication, measurements, and simulations. Both authors were involved in analyzing the data and writing the manuscript.

Notes

The authors declare no competing financial interest.

■ ACKNOWLEDGMENTS

This work is supported by a Rubicon Fellowship from the "Nederlandse Organisatie voor Wetenschappelijk Onderzoek (NWO)", as well as by the US Air Force (Grant FA9550-17-1-0331). The authors thank Majid Esfandyarpour and Søren Raza for useful discussions.

■ REFERENCES

(1) Kuznetsov, A. I.; Miroshnichenko, A. E.; Brongersma, M. L.; Kivshar, Y. S.; Luk'yanchuk, B. *Science* **2016**, *354* (6314), aag2472.

(2) Yu, Y.; Cao, L. *Opt. Express* **2012**, *20* (13), 13847−13856.

(3) Mie, G. *Ann. Phys.* **1908**, *330* (3), 377−445.

(4) Person, S.; Jain, M.; Lapin, Z.; Sáenz, J. J.; Wicks, G.; Novotny, L. *Nano Lett.* **2013**, *13* (4), 1806−1809.

(5) Staude, I.; Miroshnichenko, A. E.; Decker, M.; Fofang, N. T.; Liu, S.; Gonzales, E.; Dominguez, J.; Luk, T. S.; Neshev, D. N.; Brener, I.; Kivshar, Y. *ACS Nano* **2013**, *7* (9), 7824−7832.

(6) Fu, Y. H.; Kuznetsov, A. I.; Miroshnichenko, A. E.; Yu, Y. F.; Luk'yanchuk, B. *Nat. Commun.* **2013**, *4*, 1527.

(7) Yan, J.; Liu, P.; Lin, Z.; Wang, H.; Chen, H.; Wang, C.; Yang, G. *ACS Nano* **2015**, *9* (3), 2968−2980.

(8) Liu, S.; Vaskin, A.; Campione, S.; Wolf, O.; Sinclair, M. B.; Reno, J.; Keeler, G. A.; Staude, I.; Brener, I. *Nano Lett.* **2017**, *17* (7), 4297−4303.

(9) Kim, S. J.; Fan, P.; Kang, J.-H.; Brongersma, M. L. *Nat. Commun.* **2015**, *6*, 7591.

(10) Yu, Y.; Huang, L.; Cao, L. *Sci. Rep.* **2015**, *4*, 4107.

(11) Spinelli, P.; Verschuuren, M. A.; Polman, A. *Nat. Commun.* **2012**, *3*, 692.

(12) Spinelli, P.; Macco, B.; Verschuuren, M. A.; Kessels, W. M. M.; Polman, A. *Appl. Phys. Lett.* **2013**, *102* (23), 233902−233904.

(13) Wang, K. X.; Yu, Z.; Sandhu, S.; Liu, V.; Fan, S. *Optica* **2014**, *1* (6), 388−395.

(14) Brongersma, M. L.; Cui, Y.; Fan, S. *Nat. Mater.* **2014**, *13* (5), 451−460.

(15) Kim, I.; Jeong, D. S.; Lee, W. S.; Kim, W. M.; Lee, T.-S.; Lee, D.-K.; Song, J.-H.; Kim, J.-K.; Lee, K.-S. *Opt. Express* **2014**, *22* (S6), A1431−A1439.

(16) Decker, M.; Staude, I.; Falkner, M.; Dominguez, J.; Neshev, D. N.; Brener, I.; Pertsch, T.; Kivshar, Y. S. *Adv. Opt. Mater.* **2015**, *3* (6), 813−820.

(17) Staude, I.; Schilling, J. *Nat. Photonics* **2017**, *11* (5), 274−284.

(18) Chong, K. E.; Staude, I.; James, A.; Dominguez, J.; Liu, S.; Campione, S.; Subramania, G. S.; Luk, T. S.; Decker, M.; Neshev, D. N.; Brener, I.; Kivshar, Y. S. *Nano Lett.* **2015**, *15* (8), 5369−5374.

(19) Shcherbakov, M. R.; Neshev, D. N.; Hopkins, B.; Shorokhov, A. S.; Staude, I.; Melik-Gaykazyan, E. V.; Decker, M.; Ezhov, A. A.; Miroshnichenko, A. E.; Brener, I.; Fedyanin, A. A.; Kivshar, Y. S. *Nano Lett.* **2014**, *14* (11), 6488−6492.

(20) Miroshnichenko, A. E.; Evlyukhin, A. B.; Yu, Y. F.; Bakker, R. M.; Chipouline, A.; Kuznetsov, A. I.; Luk'yanchuk, B.; Chichkov, B. N.; Kivshar, Y. S. *Nat. Commun.* **2015**, *6*, 8069.

(21) Grinblat, G.; Li, Y.; Nielsen, M. P.; Oulton, R. F.; Maier, S. A. *ACS Nano* **2017**, *11* (1), 953−960.

(22) Liu, S.; Sinclair, M. B.; Saravi, S.; Keeler, G. A.; Yang, Y.; Reno, J.; Peake, G. M.; Setzpfandt, F.; Staude, I.; Pertsch, T.; Brener, I. *Nano Lett.* **2016**, *16* (9), 5426−5432.

(23) Smirnova, D.; Kivshar, Y. S. *Optica* **2016**, *3* (11), 1241−1255.

(24) Cao, L.; Fan, P.; Barnard, E. S.; Brown, A. M.; Brongersma, M. L. *Nano Lett.* **2010**, *10* (7), 2649−2654.

(25) van de Groep, J.; Polman, A. *Opt. Express* **2013**, *21* (22), 26285−26302.

(26) Cao, L.; Fan, P.; Vasudev, A. P.; White, J. S.; Yu, Z.; Cai, W.; Schuller, J. A.; Fan, S.; Brongersma, M. L. *Nano Lett.* **2010**, *10* (2), 439−445.

(27) Kallel, H.; Arbouet, A.; Benassayag, G.; Chehaidar, A.; Potié, A.; Salem, B.; Baron, T.; Paillard, V. *Phys. Rev. B: Condens. Matter Mater. Phys.* **2012**, *86* (8), 85318.

(28) Chong, Y. D.; Ge, L.; Cao, H.; Stone, A. D. *Phys. Rev. Lett.* **2010**, *105* (5), 53901.

(29) Zhang, J.; MacDonald, K. F.; Zheludev, N. I. *Light: Sci. Appl.* **2012**, *1*, e18.

(30) Pirruccio, G.; Lozano, G.; Zhang, Y.; Rodriguez, S. R. K.; Gomes, R.; Hens, Z.; Rivas, J. G. *Phys. Rev. B: Condens. Matter Mater. Phys.* **2012**, *85* (16), 165455.

(31) Fan, Y.; Zhang, F.; Zhao, Q.; Wei, Z.; Li, H. *Opt. Lett.* **2014**, *39* (21), 6269−6272.

(32) Zhang, J.; Guo, C.; Liu, K.; Zhu, Z.; Ye, W.; Yuan, X.; Qin, S. *Opt. Express* **2014**, *22* (10), 12524−12532.

(33) Holsteen, A.; Raza, S.; Fan, P.; Kik, P. G.; Brongersma, M. L. *Science* **2017**, *358* (6369), 1407−1410.

(34) Schwanecke, A. S.; Fedotov, V. A.; Khardikov, V. V.; Prosvirnin, S. L.; Chen, Y.; Zheludev, N. I. *J. Opt. A: Pure Appl. Opt.* **2007**, *9* (1), L1−L2.

(35) Esfandyarpour, M.; Garnett, E. C.; Cui, Y.; McGehee, M. D.; Brongersma, M. L. *Nat. Nanotechnol.* **2014**, *9* (7), 542−547.

(36) Liu, S.; Sinclair, M. B.; Mahony, T. S.; Jun, Y. C.; Campione, S.; Ginn, J.; Bender, D. A.; Wendt, J. R.; Ihlefeld, J. F.; Clem, P. G.; Wright, J. B.; Brener, I. *Optica* **2014**, *1* (4), 250−256.

(37) Wang, J.; Gudiksen, M. S.; Duan, X.; Cui, Y.; Lieber, C. M. *Science* **2001**, *293* (5534), 1455−1457.

(38) Cao, L.; Park, J.-S.; Fan, P.; Clemens, B.; Brongersma, M. L. *Nano Lett.* **2010**, *10* (4), 1229−1233.

(39) Dai, X.; Zhang, S.; Wang, Z.; Adamo, G.; Liu, H.; Huang, Y.; Couteau, C.; Soci, C. *Nano Lett.* **2014**, *14* (5), 2688−2693.

(40) Kelzenberg, M. D.; Turner-Evans, D. B.; Kayes, B. M.; Filler, M. A.; Putnam, M. C.; Lewis, N. S.; Atwater, H. A. *Nano Lett.* **2008**, *8* (2), 710−714.

DOI: 10.1021/acs.nanolett.8b01148
Nano Lett. XXXX, XXX, XXX−XXX

(41) Mann, S. A.; Oener, S. Z.; Cavalli, A.; Haverkort, J. E. M.; Bakkers, E. P. A. M.; Garnett, E. C. *Nat. Nanotechnol.* **2016**, *11* (12), 1071−1075.
(42) Lapierre, R. R.; Robson, M.; Azizur-Rahman, K. M.; Kuyanov, P. *J. Phys. D: Appl. Phys.* **2017**, *50* (12), 123001.
(43) Gu, Y.; Kwak, E. S.; Lensch, J. L.; Allen, J. E.; Odom, T. W.; Lauhon, L. J. *Appl. Phys. Lett.* **2005**, *87* (4), 043111.
(44) Hayden, O.; Agarwal, R.; Lieber, C. M. *Nat. Mater.* **2006**, *5* (5), 352−356.
(45) Bozhevolnyi, S. I.; Volkov, V. S.; Devaux, E.; Ebbesen, T. W. *Phys. Rev. Lett.* **2005**, *95* (4), 46802.
(46) Huang, L.; Yu, Y.; Cao, L. *Nano Lett.* **2013**, *13* (8), 3559−3565.
(47) Fan, P.; Yu, Z.; Fan, S.; Brongersma, M. L. *Nat. Mater.* **2014**, *13* (5), 471−475.
(48) Verschuuren, M. A.; Megens, M.; Ni, Y.; van Sprang, H.; Polman, A. *Adv. Opt. Technol.* **2017**, *6*, 243−264.
(49) Yao, H.; Yan, C. H. *J. Appl. Phys.* **1999**, *85* (9), 6717−6722.
(50) Lumerical Solutions Inc. FDTD Solutions. http://www.lumerical.com (accessed Mar 15, 2018).
(51) Palik, E. D. *Handbook of Optical Constants of Solids*; Academic, 1985.

DOI: 10.1021/acs.nanolett.8b01148
Nano Lett. XXXX, XXX, XXX−XXX